Research Square

Preprints are preliminary reports that have not undergone peer review.
They should not be considered conclusive, used to inform clinical practice,
or referenced by the media as validated information.

Electrolyte-enabled C–C cross-coupling for directed CO2-to-ethylene conversion

Xin Jia

jiaxin@shzu.edu.cn

School of Chemistry and Chemical Engineering, State Key Laboratory Incubation Base for Green Processing of Chemical Engineering, Shihezi University https://orcid.org/0000-0002-4114-8680

Ke Yi

School of Chemistry and Chemical Engineering, State Key Laboratory Incubation Base for Green Processing of Chemical Engineering, Shihezi University

Fei Zhao

College of Chemistry and Chemical Engineering Taishan University Taian

Tianwen Fang

School of Chemistry and Chemical Engineering, State Key Laboratory Incubation Base for Green Processing of Chemical Engineering, Shihezi University

Yuzhu Ding

School of Chemistry and Chemical Engineering, State Key Laboratory Incubation Base for Green Processing of Chemical Engineering, Shihezi University

Zhenyu Sun

Beijing University of Chemical Technology https://orcid.org/0000-0001-5788-9339

Yanwen Zhang

College of Sciences/State Key Laboratory of Advanced Energy Storage Materials and Technology, Shihezi University

Mei Zhang

School of Chemistry and Chemical Engineering, State Key Laboratory Incubation Base for Green Processing of Chemical Engineering, Shihezi University

Bin Yang

School of Chemistry and Chemical Engineering, State Key Laboratory Incubation Base for Green Processing of Chemical Engineering, Shihezi University

Xinghuan Liu

School of Chemistry and Chemical Engineering, State Key Laboratory Incubation Base for Green Processing of Chemical Engineering, Shihezi University

Physical Sciences - Article

Keywords:

Posted Date: May 4th, 2026

DOI: https://doi.org/10.21203/rs.3.rs-9291588/v1

License: This work is licensed under a Creative Commons Attribution 4.0 International License.
Read Full License

Additional Declarations: There is **NO** Competing Interest.

Electrolyte-enabled C–C cross-coupling for directed CO_2-to-ethylene conversion

Ke Yi[a#], Fei Zhao[b#], Tianwen Fang[a], Yuzhu Ding[a], Zhenyu Sun[a, c], Yanwen Zhang[d], Mei Zhang[a], Bin Yang[a], Xinghuan Liu[a*], Xin Jia[a*]

[a]School of Chemistry and Chemical Engineering, State Key Laboratory Incubation Base for Green Processing of Chemical Engineering, Shihezi University, Shihezi 832003, P. R. China.

[b]College of Chemistry and Chemical Engineering, Taishan University, Taian, 271000, P. R. China

[c]State Key Laboratory of Organic–Inorganic Composites, Beijing University of Chemical Technology, Beijing, 100029, China

[d]College of Sciences/State Key Laboratory of Advanced Energy Storage Materials and Technology, Shihezi University, Shihezi, Xinjiang, 832003, China.

[#] These authors contributed equally to this work.

[*]Corresponding author

Email address: liuxh@shzu.edu.cn

Email address: jiaxin@shzu.edu.cn

Abstract: Electrolyte engineering is critical for steering CO_2 electroreduction toward multicarbon products such as ethylene[1,2], yet achieving directed conversion and pathway selectivity remains challenging. Here we show an amino-functionalized ionic liquids (AFILs) electrolyte-enabled C–C cross-coupling pathway for directed ethylene synthesis on single-atom catalysts (SACs). AFILs chemically capture CO_2 as

carbamates, boosting CO production and generating high local CO coverage. The resulting carbamate-derived intermediates (–NHCO*) act as an activated C_1 partner, undergoing C–C cross-coupling with CO from SACs and thereby bypassing the need for adjacent metal sites—a key limitation for conventional C–C coupling on SACs. AFILs further stabilize critical intermediates (e.g., *OCCO, *OCCOH) through a hydrogen-bonding network and restructure interfacial water to enhance proton availability. These combined effects lower the reaction barrier while suppressing competing hydrogen evolution and methane formation. By tuning the AFIL structure (Mono- *vs*. Dual-AFIL), CO_2 conversion can be steered selectively toward ethylene, achieving a Faradaic efficiency of 80.5% at a current density of 316.2 mA cm^{-2} in flow cell. This study introduces an electrolyte-enabled C–C cross-coupling pathway that bypasses the inherent geometric constraints of SACs, opening a new route to direct CO_2 electroreduction toward valuable multi-carbon products.

Introduction

The electrocatalytic reduction of carbon dioxide (CO_2) and water (H_2O) into fuels and chemicals is a promising strategy to close the carbon cycle and store renewable energy chemically.[3,4] Among these products, the highly selective conversion of CO_2 to ethylene (C_2H_4) is desirable for its high industrial value, efficient utilization of electricity and low cost for product separation and purification.[5–7] Copper-based catalysts are the most efficient for generating multi-carbon (C_{2+}) products from CO_2. However, achieving high selectivity toward a single product of C_2H_4 remains significant challenge, primarily hampered by the complex competition among multiple side reactions.[8,9] The

rate-determining step for C_2 formation is usually the C–C coupling step, involving either dimerization of two adsorbed CO intermediates (2*CO → *OCCO) or coupling of *CO with *CHO intermediate (*CO + *CHO → *COCHO).[3] Single atom catalysts (SACs) have been thoroughly investigated in electrochemical CO_2 reduction reaction (CO_2RR) owing to the maximal atom utilization and well-defined active-site structures. SACs with M-N_4 (M = Ni, Fe, Co and Cu) structures, have shown exceptional activity and selectivity for converting CO_2 to carbon monoxide (CO)[10–13]. CO is the key reaction precursor for the formation of C_2, if these CO can be rationally utilized, increasing their coverage will be conducive to the generation of C_2H_4. However, SACs alone are notably ineffective at facilitating the crucial C–C coupling due to the lack of continuous active sites.[14] Therefore, how to overcome the active sites limitations of SACs in the C–C coupling process and achieve efficient C–C coupling on SACs is a key issue that urgently needs to be addressed.

The electrode-electrolyte interface is crucial for stabilizing intermediates such as *CO and *OCCO, and for guiding reaction pathways.[1,2,15] The electrolyte can modulate the interface, facilitating the stability and abundance of these intermediates.[16,17] Ionic liquids (ILs) are attractive electrolytes because of their high CO_2 solubility, negligible vapor pressure, broad electrochemical windows, and tunable structures.[18,19] Despite these advantages, conventional ILs are rarely designed to impose product-selective pathways: most studies report CO as dominant products, whereas C_2 products remain scarce even on Cu electrodes.[18–20] This limitation is even more pronounced on SACs, where the geometric isolation of the active sites makes the conventional coupling of the

two adsorbed *CO intermediates extremely difficult in terms of kinetics.[14] Therefore, efficient C–C coupling on SACs requires alternative pathways that bypass the need for adjacent metal sites. Recent studies have shown that amino groups can chemically capture CO_2 to form carbamates, which can directly participate in CO_2RR for CO or CH_4 formation.[21–23] We propose this hypothesis, can amino-functionalized ionic liquids (AFILs) be rationally designed to chemically capture CO_2, forming carbamate-derived intermediates (–NHCO*) during electrocatalysis, thereby enabling the in situ conversion of CO_2 into an active C_1 unit that undergoes C–C cross-coupling (–NHCO–CO) with CO from SACs? If successful, this approach would avoid the geometric challenges of SACs and allow effective C_2 synthesis on SACs. However, it remains a significant challenge to demonstrate how AFILs affect the SACs-electrolyte interface, the C–C cross-coupling intermediates and the reaction path to C_2H_4.

In this work, we have engineered two types of AFILs (1-aminopropyl-3-methylimidazolium bromide (Mono-AFIL) and 1,3-bis(2-aminoethyl)-2-methyl-1H-imidazol-3-ium bromide (Dual-AFIL))[24,25] to create tunable electrolytes that retain the key attributes of conventional ionic liquids while enabling efficient CO_2 capture through carbamate formation. These carbamates enrich CO_2 at the electrode interface and rapidly generate *CO intermediates on SACs. This significantly increases the rate of CO production compared to conventional electrolytes and establishes the foundation for C–C coupling.[26] Fig. 1a proposes an electrolyte-enabled C–C cross-coupling mechanism in which carbamate derivatives (–NHCO*) can undergo C–C cross-coupling with CO from SACs, which effectively circumvents the requirement for

adjacent metal sites that limits C–C coupling on SACs. This pathway is more efficient due to the synergistic action of the amino/carbamate groups, which stabilize key intermediates via a structured hydrogen-bonding network and remodel the interfacial water to enhance proton delivery. Collectively, these effects lower the kinetic barrier for C–C coupling and suppress methane formation and the hydrogen evolution reaction, thereby steering selectivity towards C_2H_4. Supported by comprehensive characterization and theoretical calculations, this work establishes AFILs as a powerful electrolyte design strategy. They achieve directed conversion of ethylene in SACs by electrolyte-enabled C–C cross-coupling and modulation of the electrode-electrolyte interface.

Results and Discussion

Investigation of CO_2 capture in different electrolytes and synthesis and characterization of SACs

Mono-AFIL and Dual-AFIL were subsequently synthesized according to the reported procedures (Supplementary Figs. 1-4).[24,25] Before initiating electrolysis studies, the CO_2 capture performance and accompanying structural changes of AFILs in an aqueous solution were investigated. Upon CO_2 loading, the depletion of AFIL molecules and the formation of carbamate species (predominantly the 1:2 stoichiometry product) was observed (Fig. 1b). First, the group –NHCOOH is obtained through the reaction of an amino group $–RNH_2$ with CO_2, and then the –NHCOOH is deprotonated by another amino group to form **3** in a stoichiometry of one CO_2 to two amino groups (1:2

stoichiometry).[23,26] Our experimental results showed that Dual-AFIL exhibited the highest CO_2 capture capacity (0.887 mol CO_2 (mol IL)$^{-1}$), exceeding that of Mono-AFIL as well as conventional ionic liquids (e.g., 1-aminopropyl-3-methylimidazolium bromide, CIL) and $KHCO_3$ solution (Fig. 1c and Supplementary Fig. 5). Structural changes during carbamate formation were further supported by NMR spectroscopy (Supplementary Fig. 6). The methylene protons adjacent to the amino group ($–CH_2–NH_2$) resonated around 2.3 ppm initially. Following reaction with CO_2, the electron-withdrawing effect of the formed $–NHCOO^-$ group deshielded these protons, resulting in a downfield shift to approximately 3.5 ppm ($–CH_2–NHCOO^-$).[26] Comparison of the ^{13}C NMR spectra before and after CO_2 capture revealed new resonances at 163.9 ppm and 57.5 ppm for Dual-AFIL (Supplementary Fig. 7). These correspond to the carbamate carbonyl carbon and the methylene carbon linked to the carbamate nitrogen, respectively. Additional peaks observed near the original signals are likely due to the altered chemical environments of the carbon atoms following carbamate formation. Fourier transform infrared (FT-IR) spectroscopy revealed a new peak at 1637 cm^{-1} following CO_2 exposure, indicating the formation of a new C=O group (Supplementary Fig. 8).[25] Taken together, these findings confirm the efficient and chemically specific CO_2 capture capability of AFILs, with the C=O functional group in the carbamate providing abundant reactive units for C–C coupling—a feature that warrants further investigation in electrochemical CO_2 reduction.

SACs (Ni-SAC, Fe-SAC, Co-SAC and Cu-SAC) were synthesized via a sacrificial template approach[27]. Structural and morphological characterizations (Supplementary

Figs. 9-12) revealed that the Ni-SAC has a porous two-dimensional (2D) layered architecture with a folded surface. The formation of atomically dispersed Ni sites within this 2D carbon matrix was confirmed by spherical aberration-corrected high-angle annular dark-field scanning transmission electron microscopy (HAADF-STEM) (Fig. 1d), X-ray absorption near-edge structure (XANES) spectroscopy (Fig. 1e), and extended X-ray absorption fine structure (EXAFS) analysis (Fig. 1f), with additional evidence provided in Supplementary Figs. 13-16.[28] The characterizations of Fe-SAC, Co-SAC and Cu-SAC are presented in Supplementary Figs. 17-19. This ultrathin nanosheet structure shortens electron transport pathways and increases the reaction rate, making it an ideal model for both theoretical and experimental catalytic studies.[29]

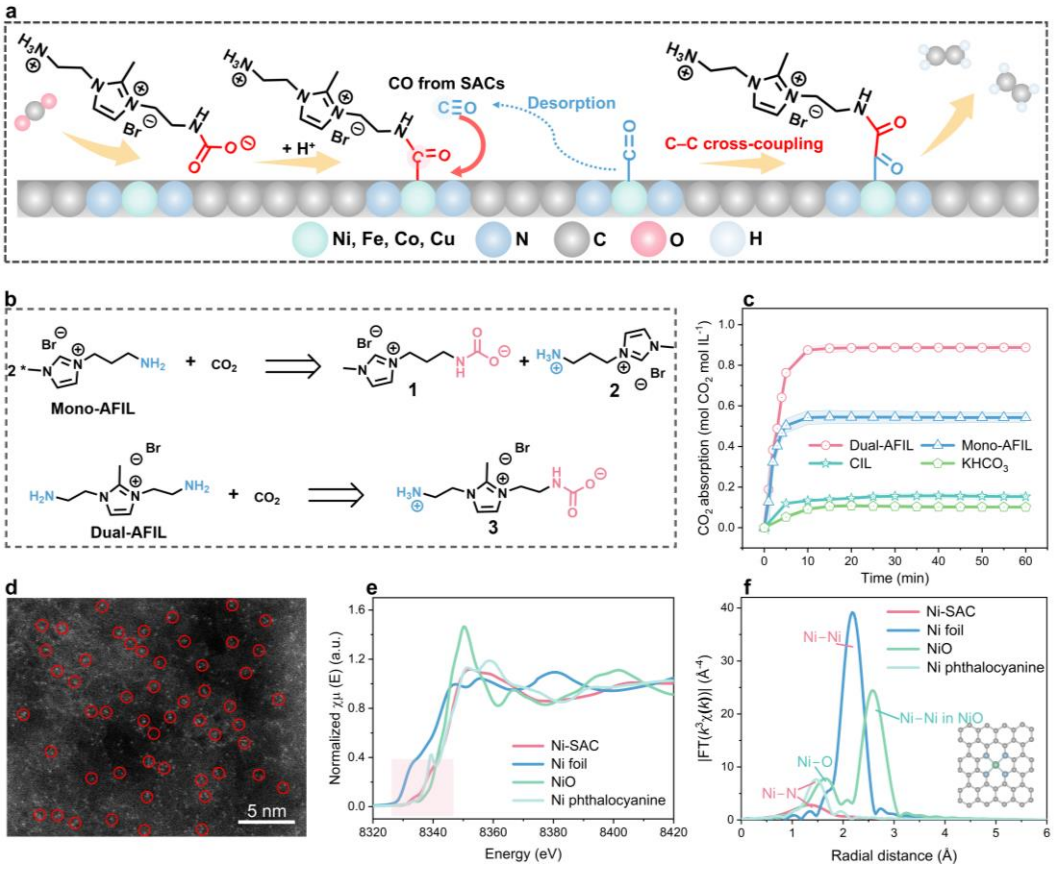


Fig. 1. (a) Schematic illustration of capture and electrocatalytic conversion of CO_2 over

144 the SACs in Dual-AFIL. (b) Reaction equations of AFILs upon bubbling CO_2. (c) CO_2
145 capture performance in Dual-AFIL, Mono-AFIL, CIL and $KHCO_3$. (d) Enlarged
146 HAADF images of Ni-SAC. Ni single atoms are marked with red circles. (e) XANES
147 spectroscopy and (f) Fourier transform (FT) at the Ni K-edge of Ni-SAC, Ni foil, NiO
148 and NiPc.

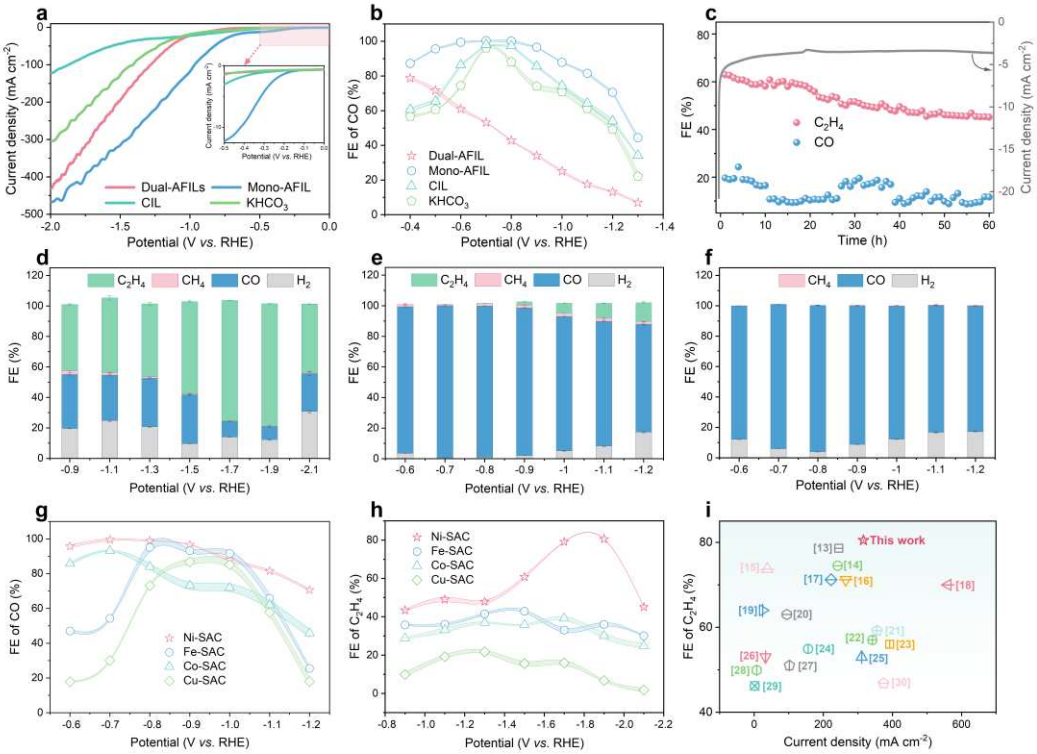
149 **Electrochemical conversion performances**

150 The CO_2RR performances were evaluated in a H-type cell equipped with a Nafion 115
151 membrane. Gaseous and liquid products were analyzed by online gas chromatography
152 (GC) and offline NMR, respectively. Linear sweep voltammetry (LSV) revealed that
153 Mono-AFIL exhibited a substantially higher current response than other electrolytes
154 (Fig. 2a),[30] indicating enhanced catalytic activity. We attribute this increase to the
155 electrochemical activation of carbamate species ($-NHCOO^-$) formed upon CO_2 capture
156 by Mono-AFIL. In contrast, Dual-AFIL showed a lower current density, which is
157 ascribed to its higher viscosity — stemming from additional amino groups — that
158 impedes ion migration and mass transfer.[25] The Faradaic currents in all CO_2-saturated
159 electrolytes significantly exceeded those in Argon (Ar)-saturated $KHCO_3$
160 (Supplementary Fig. 20), confirming CO_2 reduction as the dominant process. Product
161 analysis across a range of potentials showed that Mono-AFIL achieved exceptional CO
162 selectivity, with a Faradaic efficiency of CO (FE_{CO}) exceeding 99.9% at –0.6 V (*vs.*
163 RHE) and maintaining > 85% from –0.4 to –1.0 V (*vs*. RHE) (Fig. 2b). The stability of
164 Mono-AFIL was evaluated over 120 h of continuous operation at –0.7 V (*vs*. RHE),
165 maintaining a stable current density of 30.6 mA cm^{-2} and FE_{CO} of 95.3%

(Supplementary Fig. 21). H_2 was the only by-product, and no liquid products were detected (Supplementary Fig. 22). These results suggest that carbamate formation markedly enhances both selectivity and reaction kinetics. Conversely, Dual-AFIL shifted the selectivity toward C_2H_4, achieving a Faradaic efficiency for C_2H_4 (FE_{C2H4}) of 62.2% at –0.9 V (*vs*. RHE), while FE_{CO} dropped to 34.1% (Supplementary Fig. 23). This shift in selectivity implies that the additional amino group effectively promotes C–C coupling. Dual-AFIL also showed good stability, maintaining FE_{C2H4} > 45% over 60 h (Fig. 2c). The performance of CIL surpassed that of $KHCO_3$, achieving an FE_{CO} of 98.1% (Fig. 2b and Supplementary Fig. 24), highlighting the beneficial role of the ionic liquid environment. Kinetic analysis further shows that Mono-AFIL exhibits a smaller Tafel slope (172 mV dec^{-1}) than CIL (205 mV dec^{-1}) and $KHCO_3$ (210 mV dec^{-1}) (Supplementary Fig. 25). The turnover frequency (TOF) and CO partial current density (j_{CO}) for Mono-AFIL reached 10,209 h^{-1} and 30.4 mA cm^{-2} at –1.0 V (*vs*. RHE), significantly outperforming the control electrolytes (Supplementary Figs. 26 and 27). This demonstrates that AFILs boost the rate of CO generation, thereby creating a high local CO coverage on the electrode surface.

To overcome CO_2 mass-transfer limitations, performance was further evaluated in a flow cell.[31] C_2H_4 production (FE_{C2H4} = 0.17%) was observed at –0.8 V (*vs*. RHE) in 1 M Mono-AFIL, while C_2H_4 product was not detected in the H-type cell (Fig. 2e). With increasingly negative potentials, j_{C2H4} rose concurrently with FE_{C2H4}, reaching 124.3 mA cm^{-2} and 12.5% at –1.2 V (*vs*. RHE), respectively. This suggests that enhanced mass transport and higher CO coverage in the flow cell enable C–C coupling,

potentially via electrolyte-enabled C–C cross-coupling between surface CO and carbamate-derived C_1 fragments from AFILs. This hypothesis was strongly supported by tests in Dual-AFIL, where FE_{C2H4} reached 80.5% at –1.9 V (*vs*. RHE) (Fig. 2d), with a TOF and j_{C2H4} of 17,715.2 h^{-1} and 316.2 mA cm^{-2}, respectively (Supplementary Figs. 28 and 29). In contrast, no C_2 products were detected in CIL or $KHCO_3$ (Fig. 2f and Supplementary Fig. 30). We further generalized this behavior across SACs with different metal centers (Fe, Co and Cu), all of which produced C_2H_4 in Dual-AFIL. Crucially, a positive correlation is observed between the FE_{C2H4} in Dual-AFIL and that for FE_{CO} in $KHCO_3$ (Figs. 2g, h). This suggests that ethylene formation in Dual-AFIL is primarily governed by the SACs' intrinsic CO supply (as reflected by FE_{CO} in $KHCO_3$), with AFILs providing a unique interfacial environment that enables efficient C–C cross-coupling. Consistently, C_2H_4 selectivity also increases with the number of amino groups (Supplementary Fig. 31) and current density (Supplementary Fig. 32). As summarized in Fig. 2i and Supplementary Table 2, the C_2H_4 selectivity achieved here competes favorably with other reported systems. In summary, by creating a unique "capture-conversion" interface, AFILs steer the reaction on SACs beyond two-electron CO formation toward multi-electron, proton-coupled pathways that yield valuable multi-carbon products like C_2H_4.



206

207 Fig. 2. (a) LSV curves of Ni-SAC in CO_2-saturated 0.5 M Dual-AFIL, Mono-AFIL,
208 CIL and $KHCO_3$. (b) Plot of FE_{CO} *vs*. potential over Ni-SACs with a catholyte of 0.5
209 M Dual-AFIL, Mono-AFIL, CIL and $KHCO_3$. (c) Long-term stability of Dual-AFIL at
210 −1.0 V (*vs*. RHE) in a H-type cell. (d-f) Plot of FE of various products *vs*. potential over
211 Ni-SAC with a catholyte of 1 M (d) Dual-AFIL, (e) Mono-AFIL and (f) CIL. (g) Plot
212 of FE_{CO} *vs*. potential over SACs with a catholyte of 1 M $KHCO_3$. (h) Plot of FE_{C2H4} *vs*.
213 potential over SACs with a catholyte of 1 M Dual-AFIL. (i) Comparison of different
214 current density and FE_{C2H4} for reported works.

215 **Insights into the reaction mechanism**

216 To directly probe whether carbamates act as a carbon reservoir, we stopped CO_2 feeding
217 and purged the catholyte with Ar. The CO_2-pretreated Mono-AFIL electrolyte
218 maintained FE_{CO} > 80% within 15 hours, and CO_2-pretreated Dual-AFIL maintained

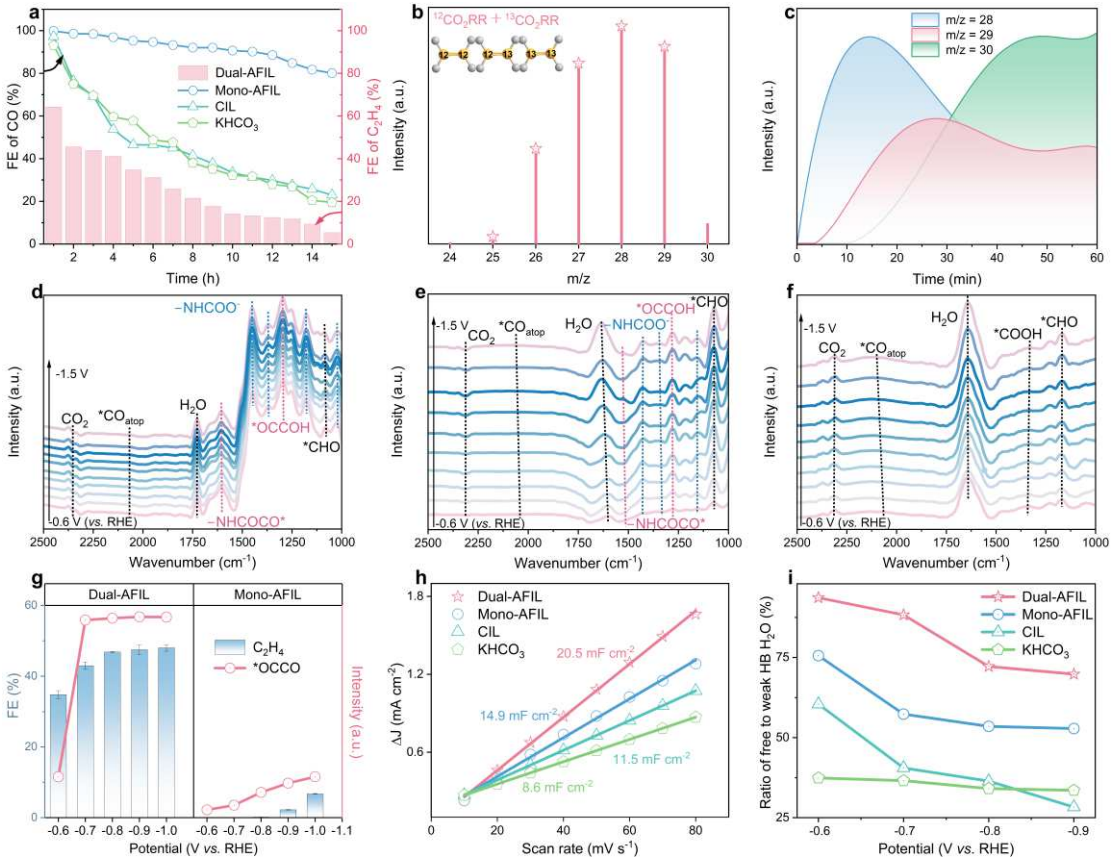
FE_{C2H4} > 30% within the first 6 hours, whereas efficiencies in CIL and $KHCO_3$ dropped rapidly (Fig. 3a). These results provide direct evidence that the pre-formed carbamate species can sustain CO_2RR as a stored carbon source. To further interrogate the identity of the C_1/C_2 intermediates and test the proposed electrolyte-enabled C–C cross-coupling mechanism, we combined isotope-labelling experiments with gas chromatography–mass spectrometry (GC-MS). A C_2H_4 standard exhibits the expected mass-to-charge (m/z) pattern (Supplementary Fig. 33), and C_2H_4 produced from $^{12}CO_2$ shows an identical set of parent and fragment ions (Supplementary Fig. 34). The dominant signal appears at m/z = 28, corresponding to $^{12}C_2H_4^+$. When CO_2RR is performed with $^{13}CO_2$, this peak shifts by +2 to m/z = 30 ($^{13}C_2H_4^+$), confirming the formation of fully labelled $^{13}C_2H_4$ (Supplementary Fig. 35). We next carried out a mixed-isotope experiment by using $^{12}CO_2$-preloaded AFILs (that is, electrolytes containing only pre-formed ^{12}C-carbamate, with excess CO_2 removed by Ar) while feeding $^{13}CO_2$ during electrolysis. In this case, in addition to the m/z = 28 and 30 peaks, a new peak emerges at m/z = 29, assigned to $^{13}C^{12}CH_4^+$ (mixed-isotope ethylene) (Fig. 3b). The appearance of the mixed-isotope product directly indicates coupling between two distinct carbon pools—pre-existing ^{12}CO and newly supplied ^{13}C-carbamate-derived carbon (–$NH^{13}CO$*) or pre-existing ^{12}C-carbamate-derived carbon (–$NH^{12}CO$*) and newly supplied ^{13}CO—consistent with an electrolyte-enabled C–C cross-coupling pathway. Notably, the m/z = 28 signal is substantially stronger than m/z = 30, indicating that ethylene formation initially draws predominantly on the pre-formed ^{12}C-carbamate reservoir. Time-resolved analysis of m/z = 28, 29 and 30 further supports this

241 interpretation (Fig. 3c). The $^{12}C_2H_4$ signal (m/z = 28) appears first, followed by the
242 mixed-isotope $^{13}C^{12}CH_4$ signal (m/z = 29), whereas the fully labelled $^{13}C_2H_4$ signal (m/z
243 = 30) increases more gradually. This temporal sequence indicates preferential
244 consumption of pre-existing ^{12}C-carbamate, followed by progressive incorporation of
245 $^{13}CO_2$ through in situ formation of ^{13}C-carbamate. As electrolysis proceeds, the ^{13}C-
246 carbamate fraction increases, leading ultimately to predominantly $^{13}C_2H_4$ formation.
247 Collectively, the isotope-dependent peak shifts, the emergence of mixed-isotope
248 ethylene (m/z = 29), and the time-evolving m/z signatures provide direct evidence that
249 carbamates serve as the reactive carbon feedstock and validate a capture and cross-
250 couple pathway as the dominant route to C–C bond formation in this system.

251 To elucidate the real-time interplay between AFILs (Mono-AFIL and Dual-AFIL)
252 and CO_2RR intermediates, *in situ* ATR-FTIR spectroscopy was employed to monitor
253 the evolution of reaction intermediates on Ni-SAC in different electrolytes across a
254 potential range of –0.6 to –1.5 V (*vs*. RHE) (Figs. 3d-f and Supplementary Fig. 36).
255 Peaks characteristic of the adsorbed –$NHCO^-$ are observed at 1018, 1180, 1370, and
256 1460 cm^{-1} (Figs. 3d, e).[23,25] Taken together, these signals confirm the chemical capture
257 of CO_2 by AFILs to form a carbamate species, which is subsequently activated to yield
258 the –NHCO*. AFILs lacked the significant peaks at 1346 cm^{-1} (*COOH) that appear
259 in the CIL spectrum (Figs. 3d-f).[32] This clear spectroscopic contrast further suggests
260 that, in AFILs, CO_2 is primarily channeled through carbamate formation rather than the
261 conventional *COOH pathway. As the applied potential becomes progressively more
262 negative, vibrational signals associated with –NHCOCO* (1598 cm^{-1}) and *OCCOH

(1289 cm^{-1}) begin to emerge and intensify in the AFILs (Figs. 3d, e). The appearance of the characteristic peak of the carbamate-derived intermediate confirmed the conjecture that the carbamate-derived CO underwent electrolyte-enabled C–C cross-coupling with the CO generated at the SACs active site. Notably, compared with Mono-AFIL, Dual-AFIL exhibits an earlier onset potential for C_2 intermediate formation and yields significantly stronger signal intensities. The observed redshift of these bands confirms that the additional amino groups in Dual-AFIL effectively stabilize these intermediates via hydrogen-bonding interactions.[33] The characteristic signals for *OCCOH and *OCCO were absent in both the CIL and $KHCO_3$ electrolytes (Fig. 3f and Supplementary Fig. 36). This contrast directly demonstrates the unique ability of AFILs to promote the formation and stabilization of these key C_2 intermediates on the electrode surface. The spectroscopic trends further link intermediate coverage to macroscopic selectivity. First, the intensity of *OCCO correlates with FE_{C2H4} (Fig. 3g), connecting surface intermediate accumulation to C_2 selectivity. Second, the increase of *OCCOH intensity with overpotential (Supplementary Fig. 37) reveals potential-dependent protonation kinetics. Third, the higher *OCCOH signal in Dual-AFIL versus Mono-AFIL directly correlates the increased amino ($–NH_2$) density with more efficient C–C coupling. The formation dynamics of gaseous products, captured by a high-speed camera at –0.7 V (*vs*. RHE), serve as a visual proxy for reaction rates. The Dual-AFIL and Mono-AFIL electrolytes (0.5 M) showed significantly more rapid bubble generation compared to CIL and $KHCO_3$ (Supplementary Figs. 38-41), providing a visual proxy for accelerated interfacial kinetics enabled by the carbamate-mediated

route. To verify electrolyte stability, the electrolytes before and after the reaction were characterized by ^{1}H NMR spectroscopy. ^{1}H NMR results of AFILs before and after electrolysis show no discernible structural changes, confirming the good stability of AFILs under CO_2RR conditions (Supplementary Fig. 22). Dual-AFIL exhibits a significantly larger electrochemically active surface area (ECSA) compared with Mono-AFIL, CIL, and $KHCO_3$, as evidenced by double-layer capacitance (C_{dl}) measurements (Fig. 3h and Supplementary Fig. 42),[34] which can further increase CO adsorption capacity and favour C–C coupling. To investigate the interfacial water structures at Ni-SAC in different electrolytes, O–H stretching modes (ν(O–H)) were measured. The ν(O–H) peak, observed in the range of 2800–3800 cm^{-1}, intensified as the potential was increased from –0.6 to –0.9 V (*vs*. RHE) due to changes in water orientation (Supplementary Figs. 43-46).[35] The FT-IR signal centered at 3200, 3350, and 3600 cm^{-1} can be assigned to strong hydrogen bond (HB) H_2O, weak HB H_2O, and free H_2O, respectively.[36] Dual-AFIL exhibits a higher fraction of free/weakly hydrogen-bonded water than the other electrolytes, and this trend persists across applied potentials (Fig. 3i). The presence of amino or carbamate structures induces the formation of disordered and loosely structured interfacial water with abundant weak hydrogen bonds/free water, which is conducive to proton transfer and enhances the ability of CO intermediates to promote C–C coupling.[37–39] Overall, the sequential evolution of key intermediate signals favoring C_2H_4 production, as captured by in situ electrochemical spectroscopy across varying potentials, corresponds well to the electrochemical properties described in the preceding section.



307

308 Fig. 3. (a) Time-dependent evolution of FE_{CO} in 0.5 M Mono-AFIL, CIL and $KHCO_3$

309 electrolytes, and of FE_{C2H4} in Dual-AFIL, were measured in H-type cell after CO_2

310 saturation was stopped. (b, c) In $^{12}CO_2$-saturated Dual-AFIL, (b) Mass spectrum of

311 C_2H_4 under $^{13}CO_2$ feeding conditions and (c) intensity trends of m/z = 28, 29 and 30

312 over time during $^{13}CO_2$ feeding. (d-f) *In situ* ATR-FTIR spectroscopy of 1 M (d) Dual-

313 AFIL, (e) Mono-AFIL and (f) CIL in the range of 1000–2500 cm^{-1} under different

314 potentials. (g) The variation trends of *OCCO peak intensity and the FE_{C2H4} in AFIL

315 and IL with respect to the potential. (h) Double layer capacity of Ni-SAC in different

316 catholytes. (i) Water structure ratio for free to weak HB H_2O for Dual-AFIL, Mono-

317 AFIL, CIL and $KHCO_3$ under different applied potentials.

318 Based on *in situ* ATR-FTIR spectroscopy and isotopic labelling experiments, a

unified catalytic picture for SACs in AFIL electrolytes emerges. Initially, CO_2 is chemically captured by AFILs to form carbamate species ($-NHCOO^-$), which are then electrochemically hydrogenated and dehydrated to yield the key surface species –NHCO*. Subsequently, CO from SACs undergoes a crucial electrolyte-enabled C–C cross-coupling reaction with –NHCO* at the active site, forming the key intermediate –NH–COCO*, which is further transformed into *OCCOH. Following C–O bond cleavage and successive hydrogenation, C_2H_4 is produced. This pathway bypasses the need for adjacent metal sites, thereby overcoming the intrinsic geometric limitation of SACs for conventional *CO–*CO coupling. To elucidate the mechanistic role of AFILs at the atomic level, we performed DFT calculations on the Ni-SAC (Supplementary Figs. 47 and 48). The Ni atom serves as the active center, hosting CO_2RR intermediates including *COOH and the carbamate-derived species –NHCO* (Fig. 4a).[22,40] Water provides protons for subsequent reduction steps. Consistent with the Tafel analysis and prior DFT studies, the rate-determining step (RDS) for CO_2RR in CIL on the 2Ni–N_4 site is $CO_2(g) \rightarrow$ *COOH, associated with an energy requirement of 1.67 eV, which limits activity. In AFILs, direct CO_2 capture as carbamate reroutes the reaction, shifting the RDS to –NH–COOH* → –NH–CO* and thereby bypassing CO_2 activation/protonation via *COOH; the barrier is reduced from 1.67 to 1.10 eV. This energetic reconfiguration rationalizes the experimentally observed activity enhancement. According to d-band theory, the projection of d orbitals on electrode surfaces governs local electron transfer and chemisorption. A more positive d-band center dictates stronger adsorption interactions between transition-metal substrates and

adsorbates, including key reaction intermediates and products.[41] The partial densities of states (PDOS) of 2Ni–N_4 in three electrolytes (Dual-AFIL, Mono-AFIL and CIL) were calculated to confirm the binding strength of the catalyst surface and the key reaction intermediate.[33] It is obvious that the d-band center is upshifted from the Fermi energy level (E_f) due to the polarization of AFILs, which shifts from –2.46 eV in CIL to –2.16 eV in Dual-AFIL (Fig. 4b). The higher d-band center of 2Ni–N_4 reveals a decrease in binding strength between active sites and *CO, which facilitates the reduction of the reaction barrier of C_2H_4 formation. We further computed the adsorption energy of CO (E_{ads}) on 2Ni–N_4, obtaining –0.41 eV (Dual-AFIL), –0.36 eV (Mono-AFIL) and –0.28 eV (CIL) (Fig. 4c). These values indicate strengthened CO binding in AFILs, most prominently in Dual-AFIL, which can increase local CO coverage and facilitate downstream C–C coupling. The adsorption behavior of CO can be further revealed by CO diffuse reflectance infrared Fourier transform spectroscopy (CO–DRIFTS). The bands at ~2118 cm^{-1} and ~2170 cm^{-1} can be attributed to gas-phase CO molecules, in which we can clearly see that the adsorption configuration of CO species is linear-type (Supplementary Fig. 49).[42] Fig. 4d shows the desorption curves of CO in AFIL, which demonstrates that CO desorbs more slowly from AFILs than from CIL, indicating stronger CO–AFIL interactions. In addition, we modeled the key reaction intermediates for C–C cross-coupling and the formation pathways of CH_4 in AFILs and CIL. These calculations build upon the key intermediates (e.g., *OCCO and *OCCOH) identified by *in situ* ATR-FTIR spectroscopy (Fig. 4e and Supplementary Figs. 50 and 51). Because CIL cannot form carbamates, it lacks an activated second carbon unit for C–C

363 cross-coupling; combined with the geometric isolation of SAC sites, this prevents
364 effective C–C bond formation and explains the absence of C_2 products in CIL (Fig. 4e
365 and Supplementary Fig. 50). In AFILs, although the barrier toward CH_4 formation
366 decreases relative to CIL (Supplementary Figs. 50 and 51), it remains higher than that
367 for C_2H_4 formation, establishing a thermodynamic preference for ethylene over
368 methane. Mechanistically, the amino sites in AFILs—particularly in Dual-AFIL—
369 chemically capture CO_2 to form carbamate species, which are rapidly
370 (electrochemically) reduced to CO, thereby creating a locally enriched and
371 continuously regenerating carbon reservoir adjacent to the Ni active site. Delivery and
372 dehydration of carbamate at the 2Ni–N_4 motif generate –NHCO*, while AFILs
373 simultaneously enhance CO coverage at the metal center. C–C coupling is then enabled
374 by dual-site cooperation: the amino/carbamate site supplies the first carbon unit and
375 couples with CO generated from Ni sites, rendering C_2 formation thermodynamically
376 accessible on an otherwise coupling-inactive SACs. Moreover, owing to its higher
377 amino-group density, Dual-AFIL forms a more extensive interfacial hydrogen-bonding
378 network, which stabilizes oxygenated intermediates (for example, *OCCO and
379 *OCCOH) and lowers transition-state energies. Furthermore, we calculated the energy
380 barrier for the C–C coupling between –NHCO* and CO. Pathway 1—involving
381 coupling between adsorbed –NHCO* and CO migrating from the metal site—shows
382 lower activation energies (0.84 eV in Dual-AFIL and 0.94 eV in Mono-AFIL) (Fig. 4e
383 and Supplementary Figs. 52 and 53) than pathway 2 (CO adsorbed on metal coupling
384 with desorbed –NHCO*) (Supplementary Fig. 54), demonstrating a stronger energetic

preference for pathway 1.

Molecular dynamics (MD) simulation was carried out for further understanding of the electrolyte-enabled C–C cross-coupling (Supplementary Figs. 55 and 56). As shown in the representative time-series snapshots (Supplementary Figs. 55), –NHCO* captures CO molecules and subsequently drives the C–C cross-coupling step. In contrast, in the absence of AFILs, CO directly desorbs from the SACs surface without reaching the catalytic active site, thereby precluding C–C coupling. The mean-square displacement (MSD) curves (Figure 4f) yield diffusion coefficients of 2.46×10^{-8} $m^2 \cdot s^{-1}$ for CO in the presence of AFILs and 1.29×10^{-8} $m^2 \cdot s^{-1}$ in their absence. AFILs enhance CO diffusion toward the catalyst surface, thereby promoting C_2H_4 production. In summary, AFILs simultaneously (i) accelerate CO_2 activation by capture-to-carbamate chemistry, (ii) increase local CO coverage through strengthened adsorption, and (iii) enable C–C bond formation by providing a cooperative adsorption site and a hydrogen-bonding microenvironment that stabilizes key intermediates. These effects overcome the intrinsic C–C coupling bottleneck of SACs and enable directed CO_2 to C_2H_4 conversion.

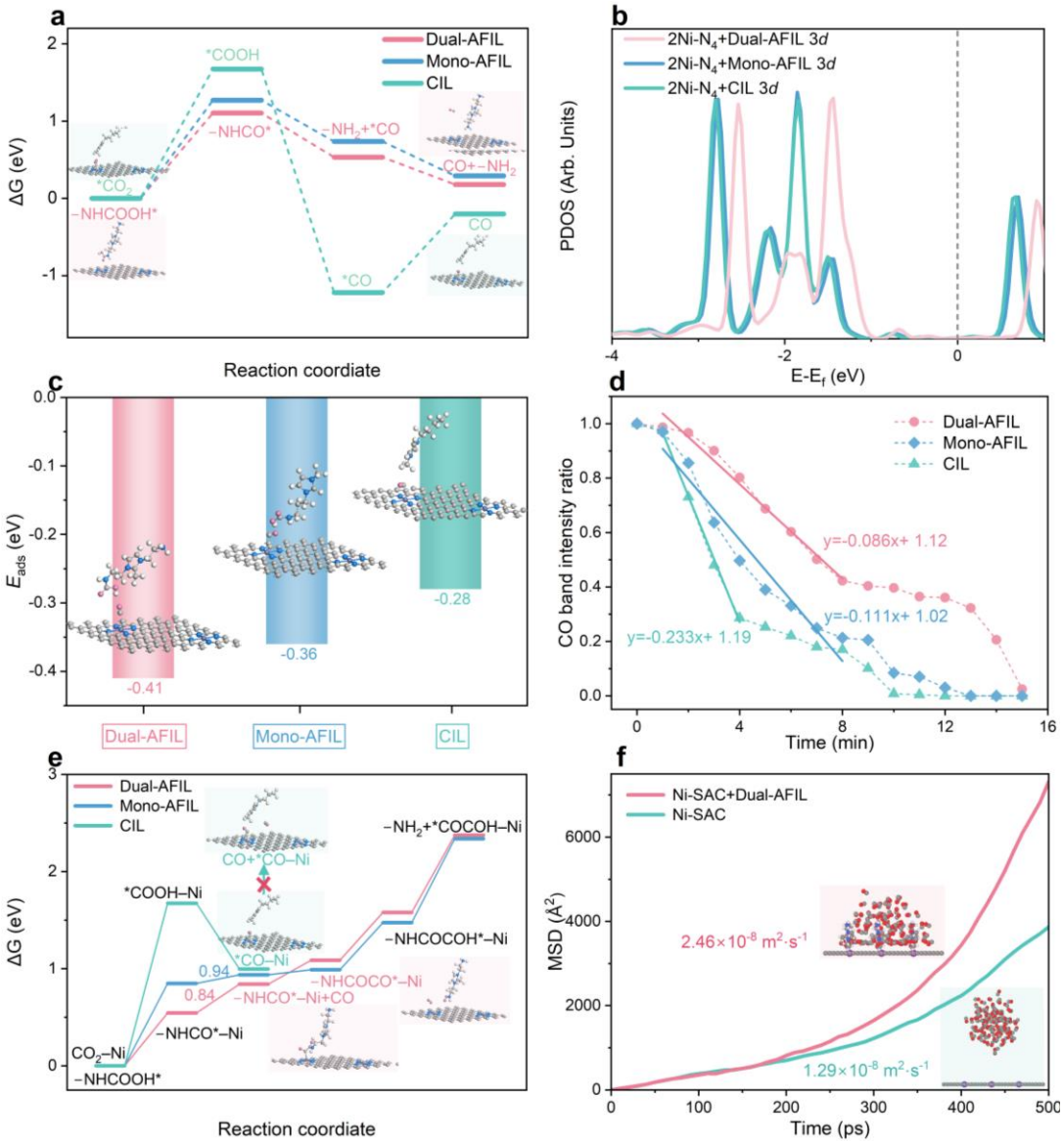


Fig. 4. Theoretical simulation. (a) The calculated free energy diagrams for CO_2-to-CO conversion in Dual-AFIL, Mono-AFIL and CIL. (b) The Eads of CO on the electrode surfaces in different electrolyte. (c) The PDOS of d orbitals of Ni atoms on 2Ni–N_4 carbon catalysts. The dashed gray line indicates the Fermi level. (d) Linear scaling relations between CO desorption curves and time based on CO–DRIFTS experiments. (e) The calculated free energy diagrams for CO_2-to-*COCOH conversion in Dual-AFIL and Mono-AFIL and CO_2-to-*CO in CIL. (f) Mean-square displacement (MSD) curves for CO over Ni-SAC and Ni-SAC in Dual-AFIL.

Conclusion

We design two AFILs as the electrolyte and identify an electrolyte-enabled C–C cross-coupling pathway in which a carbamate-derived intermediates (–NHCO*) cross-couples with CO from SACs. The electrolyte-enabled C–C cross-coupling mechanism provides a general route to overcome the geometric limitation of isolated SAC sites by introducing an electrolyte-derived C_1 unit for C–C bond formation, thereby enabling directed CO_2-to-ethylene conversion through interfacial molecular programming. This mechanism is directly corroborated by in situ spectroscopy and isotopic labelling. The AFILs serve a dual role: they enrich CO_2 as a chemical trap, raising the local CO coverage, while also establishing a tailored hydrogen-bonding network that stabilizes CO (from SACs) and key C–C coupling intermediates and restructures interfacial water to promote proton delivery. These effects lower the kinetic barrier to ethylene formation and suppress competing reactions such as hydrogen evolution. We show that product selectivity can be rationally guided through molecular design: varying the amino-group architecture (Mono- *vs*. Dual-AFIL) switches the output from near-exclusive CO (FE > 99.5%) to highly selective C_2H_4 production (FE = 80.5%) on Ni-SACs. This study demonstrates that AFILs as an active catalytic module that combines CO_2 capture with electrocatalytic conversion, establishing an electrolyte enabled C–C cross-coupling pathway for directed CO_2-to multi-carbon product conversion.

Acknowledgements

We gratefully acknowledge financial support from the Tianchi Talent Program (Young

Doctoral Program) of 2024 (CZ003117), the Foundation for High Level Talents of Shihezi University (RCZK202331), the National Natural Science Foundation of China (52073179, 52273209, 51663021, 12264042, 22308224), the Tianshan Elite Scientific and Technological Innovation Leading Talents Program of 2023 (CZ012701), the Program of Introducing Talents of Discipline to Universities (D20018), and the Natural Science Foundation of Shandong Province (ZR2023QB279). We extend our gratitude to Scientific Compass (www.shiyanjia.com) for providing invaluable assistance with the XPS and XRD analysis. We also thank Ceshigo Research Service (www.ceshigo.com) for the ICP-OES tests. We further acknowledge the use of ChatGPT 5 (OpenAI) to assist in improving the clarity and readability of the manuscript text. The authors remain fully responsible for the content and conclusions of this work.

Conflict of Interest

The authors declare no conflict of interest.

References

1. Cui, Z., Aztergo, K. D., Hwang, J. & Co, A. C. Determining CO adsorption free energies on CO_2 electroreduction active sites through kinetic analysis. *Nat. Catal.* **8**, 1117–1127 (2025).

2. Guan, Y. *et al.* Promotion of C–C coupling in the CO_2 electrochemical reduction to valuable C_{2+} products: from micro-foundation to macro-application. *Adv. Mater.* **37**, 2417567 (2025).

3. Wang, H., Kang, X. & Han, B. Optimizing CO_2 electroreduction: theoretical insights for enhancing efficiency across elementary steps. *Chem. Soc. Rev.* **54**, 10156–10244 (2025).

4. Vos, R. E. *et al.* CO_2 electroreduction on cu operates via an alternative chain growth mechanism to form C–C bonds at elevated temperature and pressure. *Nat. Catal.* **8**, 1338–1347 (2025).

5. Guo, Z. *et al.* Electrocatalytic CO_2 reduction to C_2H_4: From lab to fab. *J. Energy Chem.* **90**, 540–564 (2024).

6. Yang, Q. *et al.* Ethylene electrosynthesis at low voltages enabled by dopant-induced modulation of the rate-determining step. *Nat. Synth.* **4**, 1396–1407 (2025).

7. Zhang, R. *et al.* Cu_2O nano-homojunction for high-efficiency electrocatalytic CO_2-to-ethylene conversion. *Angew. Chem. Int. Ed.* **64**, e202501554 (2025).

8. Kok, J., Albertini, P. P., Leemans, J., Buonsanti, R. & Burdyny, T. Overcoming

copper stability challenges in CO_2 electrolysis. *Nat. Rev. Mater.* **10**, 550–563 (2025).

9. Wang, S. *et al.* Manipulating C–C coupling pathway in electrochemical CO_2 reduction for selective ethylene and ethanol production over single-atom alloy catalyst. *Nat. Commun.* **15**, 10247 (2024).

10. Zheng, T. *et al.* Large-scale and highly selective CO_2 electrocatalytic reduction on nickel single-atom catalyst. *Joule* **3**, 265–278 (2019).

11. Geng, Z. *et al.* Regulating the coordination environment of co single atoms for achieving efficient electrocatalytic activity in CO_2 reduction. *App. Catal. B: Environ.* **240**, 234–240 (2019).

12. Jiao, L. *et al.* Single-atom electrocatalysts from multivariate metal–organic frameworks for highly selective reduction of CO_2 at low pressures. *Angew. Chem. Int. Ed.* **59**, 20589–20595 (2020).

13. Wei, S. *et al.* Planar chlorination engineering induced symmetry-broken single-atom site catalyst for enhanced CO_2 electroreduction. *Nat. Commun.* **16**, 1652 (2025).

14. Chen, Y. *et al.* Recent advances in carbon-supported single-atom electrocatalysts for CO_2 reduction reaction: From dynamic evolution to structural heterogeneity regulation. *Adv. Funct. Mater.* **36**, e15847 (2025).

15. Cheng, Y. *et al.* Microenvironment tailoring for electrocatalytic CO_2 reduction: effects of interfacial structure on controlling activity and selectivity. *J. Am. Chem. Soc.* **147**, 12438–12448 (2025).

16. Qian, Z. *et al.* Hydrophobic cation-immobilized covalent organic frameworks enable selective and stable electrosynthesis of ethylene from CO_2. *J. Am. Chem. Soc.* **147**, 21877–21884 (2025).

17. Zhou, W. *et al.* Multiple tuning of the local environment enables selective CO_2 electroreduction to ethylene in neutral electrolytes. *Adv. Funct. Mater.* **34**, 2311226 (2024).

18. Rosen, B. A. *et al.* Ionic liquid–mediated selective conversion of CO_2 to CO at low overpotentials. *Science* **334**, 643–644 (2011).

19. Ratschmeier, B. *et al.* Cu/Au (111) surfaces and AuCu intermetallics for electrocatalytic reduction of CO_2 in ionic liquid electrolytes. *ACS Catal.* **14**, 1773–1784 (2024).

20. Yang, J. *et al.* Ternary ionic-liquid-based electrolyte enables efficient electro-reduction of CO_2 over bulk metal electrodes. *J. Am. Chem. Soc.* **145**, 11512–11517 (2023).

21. Bruggeman, D. F., Rothenberg, G. & Garcia, A. C. Investigating proton shuttling and electrochemical mechanisms of amines in integrated CO_2 capture and utilization. *Nat. Commun.* **15**, 9207 (2024).

22. Neves-Garcia, T. *et al.* Integrated carbon dioxide capture by amines and conversion to methane on single-atom nickel catalysts. *J. Am. Chem. Soc.* **146**, 31633–31646 (2024).

505 23. Li, P. *et al.* Tandem amine scrubbing and CO_2 electrolysis via direct piperazine
506 carbamate reduction. *Nat. Energy* **10**, 1262–1273 (2025).

507 24. Cao, K. *et al.* A selective oxidative depolymerization of larch lignin to ethyl
508 vanillate by multifunctional catalysts combining alkaline ionic liquid and
509 polyoxometalates with hydrogen peroxide. *Int. J. Biol. Macromol.* **295**, 139642 (2025).

510 25. Zhang, J. *et al.* A novel dual amino-functionalized cation-tethered ionic liquid for
511 CO_2 capture. *Ind. Eng. Chem. Res.* **52**, 5835–5841 (2013).

512 26. Li, Q. *et al.* Structure–activity relationship of a dual-function amine-based
513 electrolyte for integrated CO_2 capture and electrochemical conversion. *Chem. Eng. J.*
514 **498**, 155056 (2024).

515 27. Lu, Y. *et al.* Isolated Ni single atoms in nitrogen doped ultrathin porous carbon
516 templated from porous g-C_3N_4 for high-performance CO_2 reduction. *Nano Energy* **77**,
517 105158 (2020).

518 28. Yang, H. B. *et al.* Atomically dispersed Ni(i) as the active site for electrochemical
519 CO_2 reduction. *Nat. Energy* **3**, 140–147 (2018).

520 29. Cho, J. H. *et al.* Crystallographically vacancy-induced MOF nanosheet as rational
521 single-atom support for accelerating CO_2 electroreduction to CO. *Carbon Energy* **6**,
522 e510 (2024).

523 30. Dongare, S. *et al.* A bifunctional ionic liquid for capture and electrochemical
524 conversion of CO_2 to CO over silver. *ACS Catal.* **13**, 7812–7821 (2023).

525 31. Nguyen, T. N. & Dinh, C.-T. Gas diffusion electrode design for electrochemical
526 carbon dioxide reduction. *Chem. Soc. Rev.* **49**, 7488–7504 (2020).

527 32. Zhang, W. *et al.* Electrolyte design using "porous water" for high-purity carbon
528 monoxide electrosynthesis from dilute carbon dioxide. *Angew. Chem. Int. Ed.* **64**,
529 e202424104 (2025).

530 33. Wang, P. *et al.* Boosting electrocatalytic CO_2-to-ethanol production via asymmetric
531 C–C coupling. *Nat. Commun.* **13**, 3754 (2022).

532 34. Tan, Z. *et al.* Alkaline ionic liquid microphase promotes deep reduction of CO_2 on
533 copper. *J. Am. Chem. Soc.* **145**, 21983–21990 (2023).

534 35. Yang, C. *et al*. Bioinspired Sulfo oxygen bridges optimize interfacial water structure
535 for enhanced hydrogen oxidation and evolution reactions. *Nat. Commun.* **16**, 6459
536 (2025).

537 36. Wang, Y.-H. *et al.* In situ Raman spectroscopy reveals the structure and dissociation
538 of interfacial water. *Nature* **600**, 81–85 (2021).

539 37. Li, P. *et al.* Hydrogen bond network connectivity in the electric double layer
540 dominates the kinetic pH effect in hydrogen electrocatalysis on pt. *Nat. Catal.* **5**, 900–
541 911 (2022).

542 38. Zhang, Z.-M. *et al.* Probing electrolyte effects on cation-enhanced CO_2 reduction
543 on copper in acidic media. *Nat. Catal.* **7**, 807–817 (2024).

544 39. Zhang, H., Raciti, D. & Hall, A. S. Disordered interfacial H_2O promotes

545 electrochemical C–C coupling. *Nat. Chem.* **17**, 1161–1168 (2025).

546 40. Gu, J., Hsu, C.-S., Bai, L., Chen, H. M. & Hu, X. Atomically dispersed Fe^{3+} sites
547 catalyze efficient CO_2 electroreduction to CO. *Science* **364**, 1091–1094 (2019).

548 41. Ren, W. *et al.* Confinement of ionic liquids at single-Ni-sites boost electroreduction
549 of CO_2 in aqueous electrolytes. *ACS Catal.* **10**, 13171–13178 (2020).

550 42. Ma, F. *et al.* Steering the Site Distance of Atomic Cu−Cu Pairs by First-Shell
551 Halogen Coordination Boosts CO_2-to-C_2 Selectivity. *Angew. Chem. Int. Ed.* **63**,
552 e202412785 (2024).

553 Methods

554 Chemicals

555 Urea (> 99%), Tris (hydroxymethyl)aminomethane (> 99%), Dopamine hydrochloride
556 (> 98%), Nickel (II) chloride hexahydrate ($NiCl_2·6H_2O$, > 99.999%), Ferrum (II)
557 chloride hexahydrate ($FeCl_2·6H_2O$, > 99.999%), Cobalt (II) chloride hexahydrate
558 ($CoCl_2·6H_2O$, > 99.999%), Copper (II) chloride hexahydrate ($CuCl_2·6H_2O$, >
559 99.999%),3-bromopropylamine hydrobromide (> 98%), 2-methylimidazole (> 99%),
560 Potassium Hydroxide (KOH, > 95%), tetrahydrofuran (> 99.8%) and 1-butyl-3-
561 methylimidazolium bromide (> 99%) were purchased from Adamas. Ethanol (>
562 99.7%), methanol(> 99.5%), acetonitrile (> 99.7%) were supplied by Tianjin Concord
563 Technology Co., Ltd. 2-bromoethylamine hydrobromide (> 98%), triphenylmethyl
564 chloride (> 97%), dichloromethane (> 99.5%), triethylamine (> 99.5%), phosphoric
565 acid (> 85%), anhydrous magnesium sulfate ($MgSO_4$, > 99.5%), calcium hydride(>

97%), anhydrous N,N-Dimethylformamide (DMF, > 99.8%), sodium hydride (> 60%), hydrochloric acid (HCl, > 34%), diethyl ether(> 46.5%), sodium hydroxide (NaOH, > 98%), phosphorus pentoxide (P_2O_5) (> 99%) and potassium bicarbonate ($KHCO_3$, > 99.7%) were purchased from Aladdin. All chemicals were of analytical grade and directly used as received without further purification.

Synthesis of single-atom catalyst (M-SAC)[27]

The g-C_3N_4 template was synthesized using urea pyrolysis as previously reported in the literature. Firstly, 20 g of urea was placed in a crucible with a lid and transferred to a muffle furnace. The urea was then heated from room temperature to 550 ℃ at a ramp rate of 2.5 ℃ per minute and maintained at this temperature for 2 h in air at atmospheric pressure. Next, the nickel single atoms catalyst on nitrogen doped carbon nanosheet (Ni-SAC) was synthesized by dispersing the prepared g-C_3N_4 template (100 mg) into prepared Tris buffer solution (100 mL, 10 mmol) by sonication for 30 min, shaking every five minutes during the process. Dopamine hydrochloride (100 mg) was then added to the above solution and mechanically stirred for 3 hours at room temperature. The resulting product, named PDA@g-C_3N_4, was filtered and washed three times with deionised water. The prepared PDA@g-C_3N_4 precursor was then re-dispersed into deionised water by ultrasonication for 30 min, and 29.6 mg of $NiCl_2 \cdot 6H_2O$ was added. The mixture was stirred for 12 h at room temperature to allow chelation of Ni^{2+} with PDA. The PDA@g-C_3N_4 product (named Ni^{2+}-PDA@g-C_3N_4) anchored on PDA@g-C_3N_4 was then filtered and washed thoroughly with deionised water to remove the physisorbed Ni^{2+}. The Ni^{2+}-PDA@g-C_3N_4 was decomposed in a tube furnace at

1000 °C for 1 h under nitrogen to obtain Ni-SAC. Fe-SAC, Co-SAC and Cu-SAC were synthesized in the same way.

Synthesis of mono-amino-functionalized ionic liquid (1-aminopropyl-3-methylimidazolium bromide (Mono-AFIL))[24]

N-methylimidazole and 3-bromopropylamine hydrobromide with a molar ratio of 1: 0.8 were added to a three-necked flask and dissolved in ethanol. The reaction was carried out at 80 ℃ for 24 hours. After the reaction was completed, the excess solvent and unreacted substances were removed by vacuum distillation. A small amount of water was used to dissolve KOH and added to the reaction solution until the pH was within the range of 8-9. The remaining water was removed by distillation. The product was extracted with a mixed solvent of ethanol and tetrahydrofuran (8:2, v/v), and the filtrate was distilled and vacuum-dried to constant weight to obtain a yellow viscous liquid with a yield of 92.8%.

Synthesis of dual-amino-functionalized ionic liquid (1,3-bis(2-aminoethyl)-2-methyl-1H-imidazol-3-ium bromide (Dual-AFIL))[25]

Detailed synthesis procedures are provided in the Supporting Information.

CO_2 capture performance test

CO_2 capture experiments were conducted in a glass container (inner diameter: 2 cm), as illustrated in Supplementary Fig. 5. CO_2 gas was bubbled through the absorbent—either Mono-AFIL, Dual-AFIL, CIL, or a 0.5 M $KHCO_3$ aqueous solution—at a constant flow rate of 50 mL min^{-1}. The container was partially immersed in a water bath maintained at 20 °C to control the temperature. The mass of captured CO_2 was

610 monitored by periodically weighing the setup on an electronic balance (± 0.1 mg
611 accuracy). Absorption equilibrium was considered achieved when the weight change
612 was less than the balance's detection limit over a consecutive period. To ensure
613 weighing accuracy, the exterior of the glass container was carefully wiped dry before
614 each measurement.

615 **Electrochemical measurements**

616 **Electrocatalytic CO_2 reduction in a H-type cell.** Electrocatalytic CO_2 reduction was
617 performed in a custom gastight H-type cell with two compartments separated by a
618 Nafion 115 proton exchange membrane. A Pt mesh and a saturated Ag/AgCl electrode
619 served as the counter and reference electrodes, respectively. The electrolyte consisted
620 of a 0.5 M aqueous solution of either Mono-AFIL, Dual-AFIL, CIL, or $KHCO_3$. All
621 electrochemical measurements were carried out using a CHI 760E potentiostat (CH
622 Instruments, Inc., Shanghai, China). All potentials were measured against the Ag/AgCl
623 (saturated KCl) reference electrode and converted to the reversible hydrogen electrode
624 (RHE) scale after iR compensation according to the equation: E *vs*. RHE = E *vs*.
625 Ag/AgCl + 0.0592 × pH + 0.197 – iR_s. The solution resistance (RS) was determined
626 by electrochemical impedance spectroscopy (EIS) in the frequency range of 0.1 Hz to
627 100 kHz with an amplitude of 5 mV. Linear sweep voltammetry (LSV) was conducted
628 from 0 to –1.0 V (*vs*. RHE) at a scan rate of 10 mV s^{-1} in Ar or CO_2-saturated electrolyte.
629 Prior to each experiment, CO_2 was purged through the cathode compartment for at least
630 30 min to remove dissolved air and maintain saturation during testing.
631 Chronoamperometry was subsequently performed at each set potential for several hours.

Electrocatalytic CO_2 reduction in a flow cell. Electrochemical CO_2 reduction at high current densities was conducted using a flow cell (CX Industrial, Inc., Shanghai, China) with an electrode area of 1 cm × 1 cm. The catalyst ink was prepared by dispersing 5 mg of catalyst in a mixture of 2 mL isopropanol and 100 μL Nafion perfluorinated resin solution. This ink was then sprayed onto a 1.2 × 1.2 cm^2 piece of 25 BC carbon paper (Fuel Cell Store) using an airbrush, resulting in a catalyst loading of 0.35 mg cm^{-2}, which served as the cathode. A 2 × 2 cm^2 platinum sheet was employed as the counter electrode for the oxygen evolution reaction (OER). The cathode and anode chambers were separated by an anion exchange membrane. Both electrolytes were circulated at a flow rate of 30 mL min^{-1} using a peristaltic pump. The cathode chamber was equipped with an integrated Ag/AgCl (saturated KCl) reference electrode. CO_2 was supplied to the cathode at a flow rate of 30 sccm, and the outlet gas was directed to an online gas chromatograph (GC) for analysis. The gas effluent was analyzed every 30 minutes using a pre-calibrated gas chromatograph (GC-2014C, SHIMADZU) with high-purity Argon (Ar) as the carrier gas. A thermal conductivity detector (TCD) was used to quantify H_2, and a flame ionization detector (FID) equipped with a methanizer was used to quantify carbon monoxide (CO), methane (CH_4), and ethylene (C_2H_4). The gases employed in this study include $^{12}CO_2$ (99.999%,), $^{13}CO_2$ (99.0 at% ^{13}C), Ar (99.999%).

Measurement of electrochemical active surface area (ECSA). The electrochemical double-layer capacitances (C_{dl}) of catalysts were calculated from CV curves. The CV curves were performed at scan rates varying from 10 to 80 mV s^{-1} in the open-circuit voltage ± 0.05 V region. The capacitive currents of ΔJ (anodic-cathodic) are plotted

as a function of the CV against the scan rate. The slope of the fitting line is equal to the C_{dl}, which is linearly proportional to the electrochemical active surface area (ECSA) of the electrode.

Isotope-labelling experiments and product analysis

Isotopically labelled $^{13}CO_2$ (99.0% ^{13}C) was also used as the reactant gas. Pure $^{13}CO_2$ and mixed $^{12}CO_2$-$^{13}CO_2$ feeding experiments were carried out using the same protocol as mentioned above. Gas products were collected into a withdrawal valve after the system reached equilibrium and were injected by microsyringe into a GC-MS instrument (GC-2014C, SHIMADZU). A GC equipped with a capillary column (HP-Plot/Q+ PT, Agilent) was used for chemical separation with Ar (99.999%) as the carrier gas. The GC was interfaced with an MS (DECRA, Hiden), the data acquisition and processing were performed with MASsoft 10 Professional software.

***In situ* ATR-FTIR investigation**

In situ attenuated total reflectance–Fourier transform infrared (ATR-FTIR) spectra were acquired using a Bruker Vertex70 spectrometer equipped with a mercury cadmium telluride (MCT/B) detector and a VeeMAX III ATR accessory (Pike Technologies). A conventional three-electrode electrochemical cell was employed, utilizing an Ag/AgCl electrode as the reference and a platinum wire as the counter electrode. The working electrode was a gold film deposited on a semicylindrical silicon prism. The electrolytes employed were either 1 M Mono-AFIL, 1 M Dual-AFIL, 1 M (CIL), or 1 M $KHCO_3$ solution. During the measurements, carbon dioxide (CO_2) was continuously purged through the electrolyte at a flow rate of 20 mL min^{-1}. The electrochemical cell was

connected to a potentiostat, and constant potential electrolysis was performed from the open-circuit potential (OCP) to –1.5 V (*vs*. RHE). All spectra were collected with a resolution of 2 cm^{-1} by averaging 32 scans.

Electrochemical *in situ* CO–DRIFTS

The diffuse reflectance infrared Fourier transform spectra (DRIFTS) were recorded by a FT-IR spectrometer (Bruker VERTEX 80v) with an MCT detector (cooled by liquid N_2). For CO–DRIFTS, before introducing the reactive gas, all the samples are preheated at 120 ℃ for 1 hour to remove the possible surface residual adsorbates. Then the sample was heated to the set temperature (25 ℃), the H_2O was introduced into the cell by the flowing CO gas. Then the 3 DRIFTS data are recorded by 64 scans with a resolution of 4 cm^{-1} in K-M (Kubelka-Munk) units.

Supplementary Files

This is a list of supplementary files associated with this preprint. Click to download.

- 20260401SupplementaryFigureandtable.docx